



UNIVERSITY OF LEEDS

This is a repository copy of *Assessment of elliptic flame front propagation characteristics of iso-octane, gasoline, M85 and E85 in an optical engine*.

White Rose Research Online URL for this paper:  
<http://eprints.whiterose.ac.uk/95744/>

Version: Accepted Version

---

**Article:**

Ihracska, B, Korakianitis, T, Ruiz, P et al. (4 more authors) (2014) Assessment of elliptic flame front propagation characteristics of iso-octane, gasoline, M85 and E85 in an optical engine. *Combustion and Flame*, 161 (3). pp. 696-710. ISSN 0010-2180

<https://doi.org/10.1016/j.combustflame.2013.07.020>

---

© 2013 The Combustion Institute. Published by Elsevier Inc. Licensed under the Creative Commons Attribution-NonCommercial-NoDerivatives 4.0 International  
<http://creativecommons.org/licenses/by-nc-nd/4.0/>

**Reuse**

Unless indicated otherwise, fulltext items are protected by copyright with all rights reserved. The copyright exception in section 29 of the Copyright, Designs and Patents Act 1988 allows the making of a single copy solely for the purpose of non-commercial research or private study within the limits of fair dealing. The publisher or other rights-holder may allow further reproduction and re-use of this version - refer to the White Rose Research Online record for this item. Where records identify the publisher as the copyright holder, users can verify any specific terms of use on the publisher's website.

**Takedown**

If you consider content in White Rose Research Online to be in breach of UK law, please notify us by emailing [eprints@whiterose.ac.uk](mailto:eprints@whiterose.ac.uk) including the URL of the record and the reason for the withdrawal request.



[eprints@whiterose.ac.uk](mailto:eprints@whiterose.ac.uk)  
<https://eprints.whiterose.ac.uk/>

# Assessment of elliptic flame front propagation characteristics of iso-octane, gasoline, M85 and E85 in an optical engine

Balazs Ihracska<sup>a,\*</sup>, Theodosios Korakianitis<sup>b</sup>, Dongsheng Wen<sup>a</sup>, Paula Ruiz<sup>a</sup>, David R. Emberson<sup>a</sup>, Roy J. Crookes<sup>a</sup>, Alvaro Diez<sup>c</sup>

<sup>a</sup>*School of Engineering and Materials Science, Queen Mary University of London, UK*

<sup>b</sup>*Parks College of Engineering, Aviation and Technology, Saint Louis University, St. Louis, Missouri 63103, USA*

<sup>c</sup>*Izmir Institute of Technology, Gulbahce Campus, Izmir 35430, Turkey*

---

## Abstract

Premixed fuel-air flame propagation is investigated in a single-cylinder, spark-ignited, four-stroke optical test engine using high-speed imaging. Circles and ellipses are fitted onto image projections of visible light emitted by the flames. The images are subsequently analysed to statistically evaluate: flame area; flame speed; centroid; perimeter; and various flame-shape descriptors. Results are presented for gasoline, isooctane, E85 and M85. The experiments were conducted at stoichiometric conditions for each fuel, at two engine speeds of 1200 revolutions per minute (rpm) and 1500 rpm, which are at 40% and 50% of rated engine speed. Furthermore, fuel and speed set was tested for a higher and a lower compression ratio. Statistical tools were used to analyse the large number of data obtained, and it was found that flame speed distribution showed agreement with the normal distribution. Comparison of results assuming spherical and non-isotropic propagation of flames indicate non-isotropic flame propagation should be considered for the description of in-cylinder processes with higher accuracy. The high temporal resolution of the sequence of images allowed observation of the spark-ignition delay process. The results indicate that gasoline and isooctane have somewhat similar flame propagation behavior. Additional differences between these fuels and E85 and M85 were also recorded and identified.

*Keywords:* Flame speed, spherical, alcohol, ethanol, methanol, gasoline, optical engine

---

## Nomenclature

### Latin

$A$	area
$B$	arbitrary region
$c_V$	isochoric specific heat capacity

---

\*Corresponding author. Tel: 0044-(0)207-882-4788

Email address: b.ihracska@qmul.ac.uk (Balazs Ihracska)

$d$	infinitesimal difference operator
$da$	semi axial length
$D_F$	Feret's diameter
$f$	arbitrary function
$h$	heating value
$LHV$	lower heating value
$m$	mass
$M$	moment of a two dimensional region
$O$	parameter
$p$	pressure
$Q_{ht}$	heat transfer to walls
$r$	radius
$RNS$	roundness
$\bar{S}$	average flame speed
$SA$	semi axes of an ellipse
$Sf$	shape factor
$S_n$	flame speed
$T$	temperature
$t$	time
$U$	central moment
$u_n$	turbulent burning velocity
$V$	volume
$v_g$	gas expansion velocity
$\bar{x}$	centroid
$\bar{y}$	centroid

### Greek

$\Delta$	finite difference operator
$\epsilon$	axis orientation angle
$\eta_{Vol}$	volumetric Efficiency
$\rho$	density
$\sum$	summation operator

### Subscripts

0	spark origin
---	--------------

1, 2	integer
b	fraction burned
i	integer
maj	major
min	minor
p, w	integer
x,y,z	Cartesian coordinates, axes

#### Acronyms and abbreviations

BTDC	before top dead centre
CA	crank angle
CFD	computational fluid dynamics
CCD	charge-coupled device
CH	clearance height
CR	compression ratio
D	dimension
EoI	end of imaging period
EQR	equivalent radius
HC	hydrocarbon
rpm	revolutions per minute
RSE	relative standard error
SAFS	spherical assumption flame speed
TAI	time after ignition
TDC	top dead centre
ToI	time of ignition

## 1. Introduction

The current issues with our hydrocarbon based economy and its effects on climate change and human life are well documented (for instance [1]). These environmental and socio-political issues are among the most motivating research drivers, providing impetus for research in renewable energy and design-to-specification fuels [2–5]. Nevertheless, developed as well as developing countries still rely to a great extent on conventional fuels powering conventional engines. There is still a lot of room for considerable improvement in understanding the chemical reaction and flame-propagation processes, and reducing the emissions of these

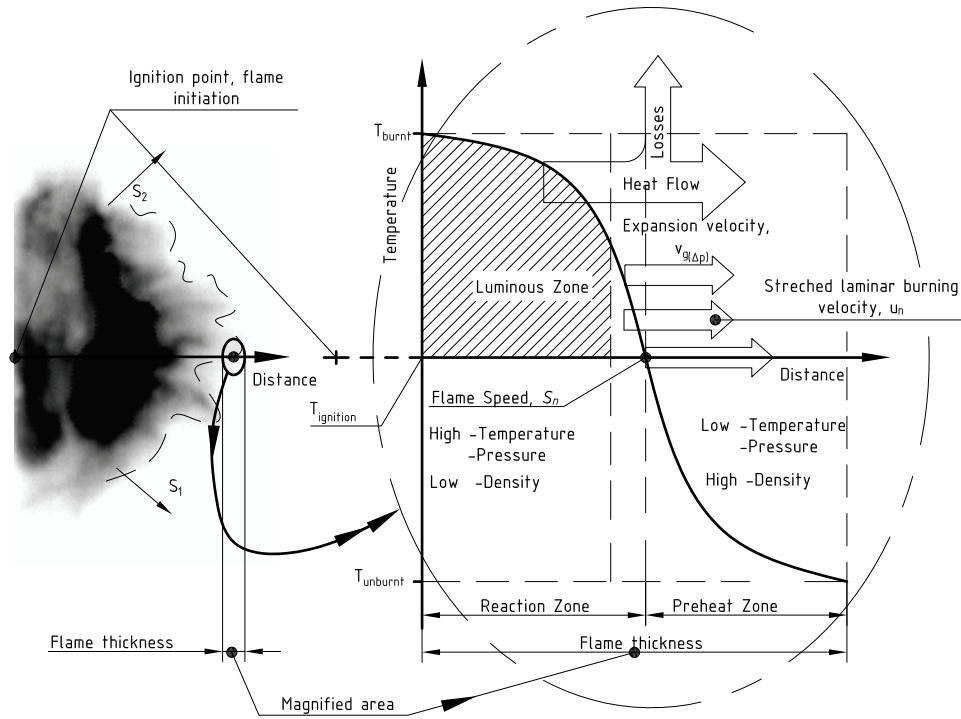


Figure 1: Illustration of the flame structure and temperature distribution of a flame, identifying the reaction and preheat zones (The image was taken at 1200 rpm, CR 5.00, with iso-octane)

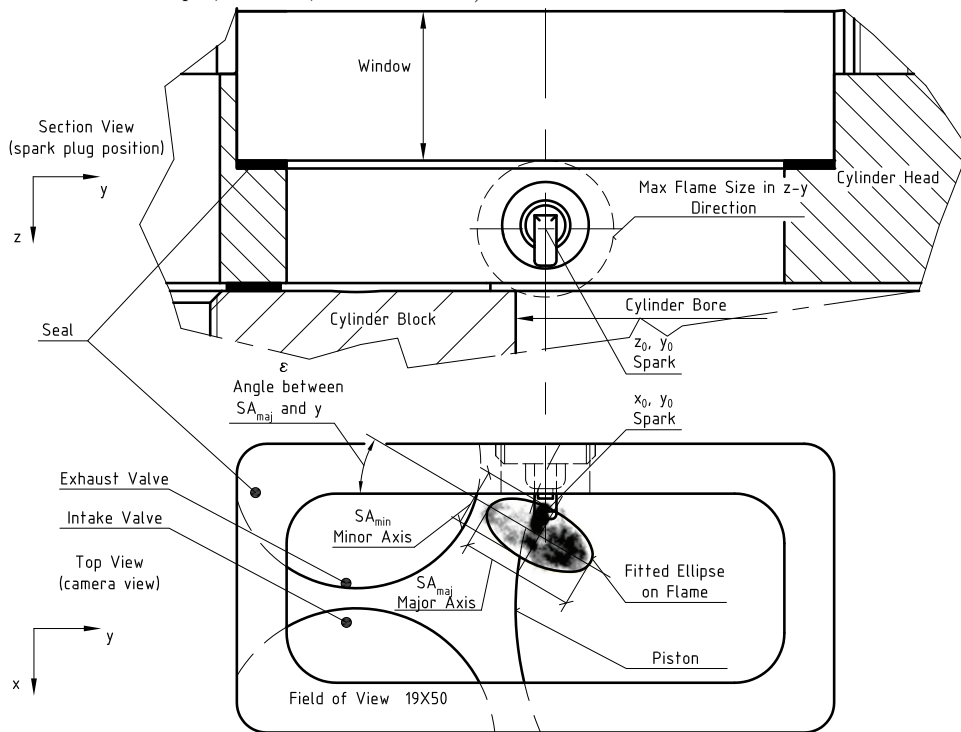


Figure 2: Section and top views of combustion chamber with fitted ellipse to the flame front

8 engine-fuel combinations. One of the most important ways to analyse combustion processes in engines is  
9 to employ 3D-CFD codes , with incorporation of various well refined fuel oxidation and flame propagation  
10 mechanisms [6, 7]. The models and codes need validation with experimental work accurately describing the  
11 exact nature of these in-cylinder processes.

### 12 1.1. Flame structure and propagation

13 Although, flame is defined as the luminous part of the burning gases caused by highly exothermic, rapid  
14 oxidation [8]. For simplicity in this study, the earliest and relatively short plasma state of the glowing charge  
15 was considered as a flame. For both moving and standing flames, the flame front is the indicator of where  
16 gases heat up and start emitting light [9, 10]. This front is considered to consist of two regions: preheat  
17 and reaction zones. For instance, Figure 1 illustrates the top view of the reaction and preheat zones in the  
18 chamber of the optical-access engine used in this paper.

19 The combustion process in SI engines can be divided into four main stages: spark and flame initiation;  
20 initial flame kernel development; turbulent flame propagation; and flame termination [11]. The first two  
21 stages are of high importance in terms of in-cylinder pressure development [12–16]. These four stages are  
22 influenced by: spark energy and duration [17]; spark plug design and orientation [18]; in-cylinder flow  
23 field [19]; cyclic cylinder charging [20]; in-cylinder composition [21]; and other related factors. A detailed  
24 literature survey on the effects of these parameters on the four stages of combustion appeared in [12].

25 The flame speed  $S_n$  (which can be measured from images of the spatial-temporal development of the  
26 flame) is given by [9, 22]:

$$S_n = v_g + u_n \quad (1)$$

27 where  $v_g$  is the gas expansion velocity immediately adjacent to the flame front and  $u_n$  is the stretched  
28 laminar burning velocity of **combusting air fuel mixture** [23]. The turbulent burning velocity equals the  
29 laminar velocity with the added effect of the flow field, geometry; wrinkling of the flame front; pressure  
30 effects on flame thickness; history of the flame [24]. The effect of the turbulent flow field is crucial for the  
31 first and second stage of combustion. It has been shown that the smallest flame kernels are distorted shortly  
32 after ignition [25]. The laminar velocity is an intrinsic property of a combustible fuel, air and burned gas  
33 mixture. That is defined as the velocity, relative to and normal to the flame front, with which unburned gas  
34 moves into the front and is transformed to products [26].

35 Turbulent burning velocity plays a prime role and directly effects the in-cylinder pressure development,  
36 i.e., engine performance. **Turbulent burning velocity are laminar burning velocity are important physical**  
37 **properties of fuel air mixtures. It is essential that both of these velocities are derived experimentally from**  
38 **flame speed and area of in-cylinder pressure measurements [9, 11, 14, 22].** The work produced by an engine  
39 is related to the flame speed as can be inferred from the following. The burned mass of charge is given by

$$m_b(t) = (\bar{S}_x \bar{S}_y \bar{S}_z)(t) \rho_b(t) S f(t), \quad (2)$$

where  $\bar{S}_x$ ,  $\bar{S}_y$ ,  $\bar{S}_z$  are the average flame speeds in the  $x$ ,  $y$ ,  $z$  directions. These can be determined by dividing the flame radius along an axis by the elapsed time from ignition.  $S f$  is a shape specific function. The burning of fuel releases energy to the working fluid in the cylinder, given by [4, 26]:

$$m_b LHV - (mc_V dT) - \Sigma h_i dm_i - dQ_{ht} = pdV \quad (3)$$

The rate of burning of the air-fuel mixture affects the chemical energy change of the fluid, and this directly affects the indicated work and power output. In equation 3 the work done on the piston  $pdV$  equals the energy released from the burning fuel  $m_b LHV$ , minus the energy required to heat up the charge  $mc_V dT$ , minus the heat transfer to walls  $dQ_{ht}$ , and adjusted by the masses leaving or entering the chamber  $\Sigma h_i dm_i$ . Note: term  $\Sigma h_i dm_i$  can be positive (during fuel injection) or negative (flow to crevice volumes or blow by). Therefore engine performance is highly dependent on flame propagation characteristics within the cylinder.

### 1.2. Visualisation of initial flame kernel growth in SI engines

In previous engine research images of flames in cylinders showed a significant enflamed volume, but the pressure measurements were not accurate or sensitive enough to indicate the evolving flame kernels [15, 21]. Therefore, optical investigation of combustion is preferred to pressure tracing at the early combustion stages. The practical realization of visual access to a combustion chamber of a working piston engine is not easy, with any of the visible, ultra violet spectra or laser radiation approaches [43–46]. The fluctuating pressure at high temperature, the limited strength of transparent materials and the geometrical constraints kept investigators from studying optical engines at real working conditions. In most cases the engine speed and CR were kept low in order to observe the propagating flames. In previous investigations the effect of changing engine speeds and equivalence ratios were studied. However, because of the tight cylinder geometries, there has been no optical data recorded in the same engine at different compression ratios. Another major difficulty is the time scale of rapid oxidation. The average of temporal resolution that can be found in the literature is about 0.2 to 0.4 ms. Only one paper included data at higher temporal resolution, which could potentially provide insight to the earliest and faintest flames [32]. It has also been reported that fouling of the optical ports limits the length of operation time [18]. The experimental conditions and a general summary of the most relevant work on flame speed measurements and other investigations in optical engines can be found in Table 1. A comprehensive review of experimental investigation techniques in reciprocating-piston engines is in [47].

It has been shown that the shape of the evolving flame kernel has a major effect on the in-cylinder combustion processes [14]. Generally, previous studies have assumed that the propagation of the spark-initiated oxidation is isotropic, i.e. spherical flame propagation [15, 16, 18, 21, 25, 28–36, 38, 39]. Only a

Table 1: Table of prior related publications

Research		Imaging				Engine		
Author	Ref.	Method	Method Detail	Frame rate (f/s)	Speed (rpm)	Fuel	A/F	CR
Rashidi	[27]	Luminous	high speed consecutive images	2000	1096	isooctane	1.08	-
Berreta	[21]	Luminous	high speed imaging, hand traced, NaCl seeding	5000	872, 1233	isooctane	1.13-0.98	7.86
Heywood	[28]	Schlieren	each picture is from different cycle	1380	1380	propane, hydrogen	1.00	7.00
Gatowski	[29]	Schlieren	high speed consecutive images	2000	740, 1400	propane	0.9	5.75
zur Loye	[25]	2D visual.	laser scattering, TiO <sub>2</sub> , ZrO <sub>2</sub> seeding	-	300-3000	propane	1.0, 0.5	8.00
Keck	[15]	Schlieren	high speed consecutive images, hand traced	2000	1400	propane	0.87	5.75
Pischinger	[16]	Schlieren	high speed consecutive images	25000	1400	propane	1.00, 0.77, 0.71	6.70
Bates	[13]	Luminous	multi exposure in one frame	30 (NTSC)	500	propane	0.6-0.9	9.10
Nakamura	[30]	Luminous	high speed consecutive images	10000	1500	gasoline	1	9.30
Herweg	[31]	Schlieren	pictures are from different cycle	flash light, pulse 40ns	800-2000	propane	0.77	7.30
Bates	[14]	Luminous	multi exposure in one frame	30 (NTSC)	500, 1000	propane	0.75	9.10
Shen	[32]	Schlieren	high speed consecutive images, hand traced	20000	500, 1100	isooctane	1.00-0.91	7.70
Aleiferis	[18]	Luminous	double-exposed images	25	1500	isooctane	0.68	7.90
Aleiferis	[33]	Luminous	double-exposed images	25	1500	isooctane	1.00, 0.68	7.90
Lee	[34]	Laser deflection & Schlieren	comparison between the 2 methods	3000	1200, 1500, 1800	liquefied petroleum gas	0.80, 1.10, 1.30	10.00
Conte	[35]	Optical and ion sensors	mapping (no images taken)	-	2000	gasoline and gas mixtures	1.00	8.70
Gerke	[36]	OH-chemiluminesc.	high speed imaging	10000	compression machine	hydrogen	0.36-2.50	(p=5-45 bar)
Bates	[13]	Luminous	multi exposure in one frame	30	500	propnae	0.70	9.00
Tahtouh	[37]	Luminous	high speed imaging	6000	1200, 2000	isooctane, methane	1.00, 0.80	9.50
Baritaud	[38]	Schlieren	high speed consecutive images, hand traced	6000	500, 1040	propane	0.65, 0.85	6.00
Tagalian	[39]	Z-Schlieren	5 cycles analysed	1400	1400	propane	0.90	-
Aleiferis	[40]	Shadowgraphy	high speed, consecutive pictures, 100 cycles	9000	1500	E85, gasoline	1.00	11.15
Aleiferis	[41]	chemiluminesc.	high speed, consecutive pictures, 100 cycles	9000	1500	alcohols, HCs	1.00	11.15
Herweg	[42]	Luminous	experimental work in a side chamber and one-dimensional model	-	300, 500, 750, 1000, 1250	propane	1.00, 0.77, 0.67	7.30



Table 2: Fuel properties

Fuel	Formula	Molar	Density	Lower	Stoichiometric	Flammability	
		Mass		Heating	A/F ratio	limits in air	
		Value			(V%)		
	-	(g)	(kg/m <sup>3</sup> )	(MJ/kg)	(kg/kg)	lower	upper
Gasoline (approx.)	C <sub>n</sub> H <sub>1.87n</sub>	110	720-780	44.2	14.60	1.0	8.0
Isooctane	C <sub>8</sub> H <sub>18</sub>	114.23	692	44.3	15.13	1.0	6.0
Ethanol	C <sub>2</sub> H <sub>6</sub> O	46.07	785	26.9	9.00	3.3	19.0
Methanol	CH <sub>4</sub> O	32.04	792	20.0	6.47	6.0	36.0
E85	C <sub>n</sub> H <sub>2.88n</sub> O	56.29	771	29.6	9.92	3.0	17.1
M85	C <sub>n</sub> H <sub>3.74n</sub> O	44.37	777	23.6	7.77	5.3	31.5

few studies mentioned different flame-front geometries [14, 15, 30, 39] and looked into implications arising from the assumption that the flame front surface had a spherical geometry. However, these shapes were not described mathematically and detailed analyses were not carried out.

Even though the in-cylinder flame front is a three-dimensional flame, in most studies flame-speed measurements are measured from two-dimensional projections of the images. Applying the isotropic propagation assumption, the two-dimensional projected contours of spherical flames can be digitized and their various geometrical properties determined. Actual flame speeds and flame shapes were measured in a small number of studies, where the flame radii were calculated using the “equivalent radius” (EQR) method [15, 16, 25, 32, 33, 38–41], which determines the radius from the measured area:

$$r = \sqrt{\frac{A}{\pi}} \quad (4)$$

where  $r$  is the flame radius and  $A$  is the area of the projected region. There has been no attempt to refine this assumption.

Many of the early investigators (that established the fundamentals of optical engine work) due to limitations of available tools used hand tracing methods to delineate the boundaries and/or had low number of samples (3 to 6 measurements averaged) [19]. Later papers do have a larger number of measurements, but statistical distribution of their findings was not documented [37]. Cyclic variability in engines is a widely studied phenomenon [12, 18, 27, 48]: the nature of the processes prior to ignition, the ignition itself and combustion instabilities cause fairly high standard deviation of in-cylinder measurements. Therefore statistical tools and high numbers of samples are needed in order to keep errors in the results low.

In previous studies with optical-access engines the main choice of fuels were pure hydrocarbons (HC), such as propane and isooctane. Less attention was paid to practical fuels such as gasoline and alcohol blends (Table 1). It is a usual practice to use isooctane as a surrogate of gasoline in engine related research purposes as these two fuels have similar physical properties. Moreover, gasoline is a mixture of hydrocarbons with a composition that is not guaranteed, whereas isooctane is an easily available pure chemical. Previous

93 flame-propagation studies in optical engines did not compare flame propagation characteristics of gasoline  
 94 and isooctane to verify the two fuels behaved in a similar fashion. Alcohols and blends with gasoline (or  
 95 isooctane) have been used in piston engines since the engine itself was invented. At present, bio-alcohols  
 96 are proposed among the candidates for future fuels. Many studies have investigated their emission and  
 97 performance qualities [40, 49–52], but the literature is lacking the relevant optical-engine data. Usually each  
 98 published study concentrates on one engine geometry (e.g. one compression ratio) and one fuel. There are  
 99 very few optical data available on comparison of different fuels in the same engine operating conditions.  
 100 Table 2 lists some of properties of the fuels tested in these engines (from [26, 53]).

### 101 1.2.1. Current contribution

102 The main contribution of this paper is statistical characterization of non-spherical and non-isotropic  
 103 aspects of flame propagation. A specifically-designed multi-fuel optical engine was used to compare flame-  
 104 propagation characteristics of isooctane and gasoline. E85 and M85 were also investigated as practical  
 105 alternative spark-ignition engine fuels and to fill in the gaps in the flame-propagation data base. E85 and  
 106 M85 were “research grade”: they were mixed in house using pure alcohols and isooctane. CR of 8.14:1  
 107 and 5:1 were chosen to test the fuels: the higher to simulate real engine conditions; and the lower one to  
 108 provide sufficient contrast from the higher one. Utilizing the capability of an extremely sensitive and fast  
 109 camera, high temporal resolution was achieved, allowing investigation of phenomena like ignition delay and  
 110 early flame kernel formation. The large number of samples allowed mathematical statistics to be used to  
 111 find the typical distribution of the measured data. It was concluded that elliptical flame structures describe  
 112 flame propagation more accurately than spherical flame structures in many cases. Therefore a new and  
 113 more detailed set of combustion data with these fuels has been obtained, and it can be used for validation  
 114 of CFD and emissions studies.

Table 3: Engine data

Description	Value
Make	Briggs & Stratton
Model NO.	093432
Type	4-Stroke, Air Cooled, Wet Sump
Valve, Head Arrangement	2-Valve, L-head
Bore x Stroke (mm)	65.1 x 44.4
Connection Rod Ratio	0.25
Displacement (cm <sup>3</sup> )	148
Field of View (mm)	19 X 50
Compression Ratios	5.00, 8.14

## 115 2. Experimental apparatus and imaging system

### 116 2.1. Engine and optical access

117 Experiments were carried out in a modified single cylinder four-stroke Briggs & Stratton engine. Some  
118 parameters of the engine are shown in Table 3. Many properties of this research engine are comparable  
119 with commercial engines. The engine original lubrication and cooling systems, the valve train, and timing  
120 were not modified. The exhaust muffler was taken off and the exhaust port was connected straight into  
121 a laboratory extractor. The nozzle of the original carburetor was replaced with a variable area nozzle,  
122 so that any air-fuel mixture could be set by varying the fuel and/or air flow. The fuel flow and air flow  
123 were measured electronically. The volume change of the fuel stored in a small tank above the carburettor  
124 was measured, and the fuel flow rate was determined with known fuel density. The air consumption was  
125 measured using an orifice plate based on the Bernoulli's principle, Figure 3. The measurement was taken  
126 every 0.5 second, and the air/fuel ratio was calculated subsequently. During the whole operation period of  
127 the engine, the air/fuel ratio was monitored to keep a constant air/fuel ratio.

128 The rig had a 12 V ignition system containing a BOSCH K12V TCI coil to supply high voltage to the  
129 NGK CHSA spark plug. The geometry of the plug had to be modified in order to fit in the cylinder head.  
130 The thread, sealing mode and electrical connection had to be changed, however, the electrodes and their  
131 gap of 0.7 mm was not altered. The ignition timing was kept the same, 20 CA degree BTC, for all fuels and  
132 operating conditions. Therefore, at the time of ignition the flow field adjacent to the spark was similar for  
133 the tested fuels at a given operating point. The position and orientation of the spark plug is illustrated in  
134 Figure 2, and the azimuthal orientation of the spark-plug gap was kept constant in all the experiments. The  
135 optical access was gained by a specifically designed cylinder head. The chosen Briggs & Stratton engine had  
136 an air cooled and side valved configuration, which resulted a simpler head design. One of the main design  
137 goals was to keep the compression ratio close to ones that real engines have. This restricted the maximum  
138 achievable size of field of view. The location and size of optical access was found by ensuring that some  
139 portion of the valves and piston were visible and the spark plug placed in the middle. Finally, required grades  
140 of materials, minimum wall thickness and cooling surface were determined by Finite Element Analysis. The  
141 final version of the research head had similar internal and outer geometrical design to the original one, but  
142 the compression ratio became variable using spacers from 5.00 up to its maximum value 8.14.. The detailed  
143 in-cylinder geometry is illustrated in Figure 2.

144 Prior to image recording the engine was heated up using a metal blank instead of the window, which  
145 was also pre-heated by a blower torch. The design of the window clamp allowed swapping the blank to  
146 the window in a few seconds preserving the temperature of the system. Then, the engine was run an  
147 additional 5 minutes to reach steady operating conditions. For statistical analyses over 100 sets of data  
148 were obtained at each engine operating point. The camera memory could only store about 30 sets of data

149 at a time. Therefore each time about 30 sets of data were recorded, and while the engine was running at  
 150 the same operating point the camera memory was copied to the computer over about 30 seconds. Then  
 151 a subsequent set of about 30 data points was obtained, and the process was repeated four times at each  
 152 operating point. The computer code had a comparison loop that compared the four series of data to each  
 153 other to check the stability of conditions and to look for contamination on the window. The important  
 154 factors influencing the initial flame development are summarized in Table 4. The volume of the combustion  
 155 chamber is calculated by the clearance heights as the piston movement is quite small during the initial flame  
 156 propagation period. As it is difficult to obtain accurate values for residual gas volume, it is estimated by  
 157 using valve timing and clearance volumes, and neglecting the effects of swinging gases. Thermodynamic  
 158 conditions were recorded during the tests but were not synchronised with visualisation, soonly the mean  
 159 values are given in Table 4. Each fuel had slightly different pressure curve at compression stroke, but the  
 160 differences were smaller than the measurement errors. The computer code could only measure the spark  
 161 duration when there was no combustion inside the engine (in dark) as it could not distinguish between flame  
 162 and spark. During the experiments, it was found that the spark length was significantly shorter when there  
 163 was combustion around it. So the spark length shown in Table 4 was derived from manual analysis of ten  
 164 randomly chosen combustion images.

Table 4: Details of operating conditions

	Engine speed (rpm)	CR	Value
Clearence Height (mm) at ToI / EoI	1200	5.00	32.10 / 30.74
		8.14	14.76 / 13.40
	1500	5.00	32.10 / 30.57
		8.14	14.76 / 13.23
Est. Residual Gas Volume Fraction (%)		5.00	25
		8.14	14
Volumetric Efficiency (%)	1200		27.02±(1.35)
	1500		27.93±(1.40)
Pressure at Time of Ignition (bar)	1200	5.00	3.78±(0.19)
		8.14	6.29±(0.31)
	1500	5.00	3.97±(0.20)
		8.14	7.41±(0.37)
Spark Duration (ms)			1.48±(0.19)

165 It is believed that this optical engine provided a similar description of real engine processes to production  
 166 engines as other optical engines. The main disadvantage of the designed configuration is the different in-  
 167 cylinder flow field from the usual pent-roof type 4-stroke automotive engines. On the other hand, the  
 168 unmodified wet-sump lubrication allowed running the engine at normal operating temperatures without  
 169 further modifications. At this temperature there was no fuel or oil condensation on the window to cause  
 170 fouling. Fouling has been reported as one of the constraints limiting other optical-access engines. Less

171 contamination on windows provided prolonged firing periods and clearer images.

## 172 2.2. Fitting an ellipse to an arbitrarily shaped region

173 A fundamental task of automated image analysis and computer vision techniques is to fit geometries to  
174 regions or set of points. In two-dimensional space the most primitive approach to model a 2D shape is to  
175 fit a circle. The next level to retrieve more information from the model is to fit an ellipse, which (unlike  
176 a circle) is not symmetrical about every one of its diameters. In this work ellipses are used to model and  
177 analyse the non-isotropic propagation of in-cylinder flames.

### 178 2.2.1. Fitting methods

179 Fitting an ellipse to an arbitrarily shaped region has been studied in considerable detail. There are two  
180 basic methods for fitting ellipses: (1) boundary-based and (2) region-based methods. Detailed descriptions  
181 of these can be found in [54–56].

182 Boundary-based methods consider that the arbitrary region consists of a set of points sampled from the  
183 region. Prior research in image analysis and computer vision have employed a variety of techniques including  
184 linear least squares, weighted least squares, Kalman filtering and robust estimation methods [54, 57]. Region-  
185 based methods are frequently used in image processing and were chosen here to determine some geometric  
186 characteristics of flames. These methods are detailed by Gonzales and Wintz [55]. They use the moments  
187 of a region in calculating the best-fit ellipse [56, 58, 59], and equalize the second order moment of a region  
188 in order to determine the best-fit ellipse. In the case of regular shapes ( i.e., region close to an ellipse)  
189 the aforementioned methods show no major difference in the result. For in-cylinder flames, region-based  
190 methods are more appropriate as they are less affected by boundary irregularities.

### 191 2.2.2. Determining flame speed from fitted ellipses

192 The moment of  $(w + q)$  order of a 2 dimensional arbitrary region ( $B$ ) is given by [60].

$$M_{wq} \equiv \int \int_B f(x, y) x^w y^q dx dy \quad (5)$$

193 calculated over  $B$ . For regions where no properties are varied, function  $f$  has a value of unity. When  $(w + q)$   
194 equals zero, i.e., the zeroth moment is the area of region  $B$ , the centroids are given by the quotient of the  
195 first and zeroth moments:

$$\bar{x} \equiv \frac{M_{10}}{M_{00}} \quad (6)$$

$$\bar{y} \equiv \frac{M_{01}}{M_{00}} \quad (7)$$

196 Then, the central moments can be determined evaluating the following integral:

$$U_{wq} = \int \int_B f(x - \bar{x})^w (y - \bar{y})^q dx dy \quad (8)$$

197 or can be written in terms of moments:

$$U_{00} = M_{00} \quad (9)$$

$$U_{10} = U_{01} = 0 \quad (10)$$

$$U_{20} = M_{20} \frac{M_{10}^2}{M_{00}} \quad (11)$$

$$U_{02} = M_{02} \frac{M_{01}^2}{M_{00}} \quad (12)$$

$$U_{11} = M_{11} \frac{M_{10}M_{01}}{M_{00}} \quad (13)$$

198 Finally, the best-fit ellipse can be determined using the central moments:

$$O \equiv \sqrt{4U_{11}^2 + (U_{20} - U_{02})^2} \quad (14)$$

$$\epsilon = \frac{1}{2} \tan^{-1} \left( \frac{2U_{11}}{U_{20} - U_{02}} \right) \quad (15)$$

$$SA_{maj} = \sqrt{\frac{2(U_{20} + U_{02} + O)}{U_{11}}} \quad (16)$$

$$SA_{min} = 2\sqrt{\frac{2(U_{20} + U_{02} - O)}{U_{11}}} \quad (17)$$

199 where  $SA_{maj}$ ,  $SA_{min}$  and  $\epsilon$  are the semi-major, minor axes and the orientation angle respectively. In this  
 200 work bitmap images were acquired from the high-speed camera. These were converted to pixelated images  
 201 from which the central moment integral were obtained from:

$$U_{20} = \frac{1}{n} \sum_{i=1}^n (x_i - \bar{x})^2 \quad (18)$$

$$U_{02} = \frac{1}{n} \sum_{i=1}^n (y_i - \bar{y})^2 \quad (19)$$

$$U_{11} = \frac{1}{n} \sum_{i=1}^n (x_i - \bar{x})(y_i - \bar{y}) \quad (20)$$

202 and can be fairly easily calculated using a computer code.

### 203 2.2.3. Flame speed derived form optical data

204 Once the semi-major and minor axes were calculated for each image, the difference in their length was  
 205 determined by:

$$\Delta da(t) \equiv da_t - da_{t-1} \quad (21)$$

206 where in this case  $da$  is  $SA_{maj}$  or  $SA_{min}$ . Dividing the change in length with the known time interval gives  
 207 the flame **speed** at the given time:

$$S_n(t) = \frac{\Delta da(t)}{\Delta t}. \quad (22)$$

208 *2.2.4. Shape factor*

209 There are many ways to arrange geometric parameters of a shape non-dimensionally. Details of shape de-  
 210 scriptors can be found in [56]. Usually geometric regions are circular when their descriptor value approaches  
 211 unity. Here the shape evolution of  $SA_{maj}$  and  $SA_{min}$  are of interest. Their most suitable descriptor is round-  
 212 ness  $RNS$ , which does not vary with the boundary irregularities (local shape wrinkles or disturbances).

$$RNS \equiv \frac{4A}{\pi D_F^2} \quad (23)$$

213 where  $RNS$  is the large scale shape factor,  $A$  is the area of a region and  $D_F$  is Feret's diameter, the longest  
 214 distance between any two points along the boundary of a region.

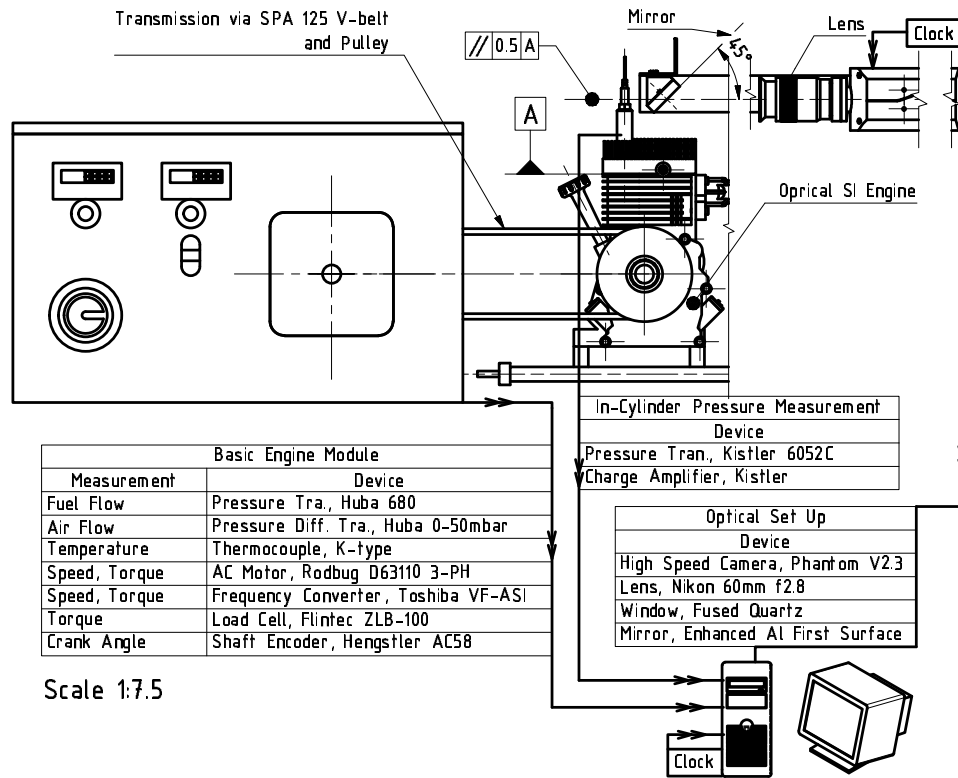


Figure 3: Schematic of the experimental rig: layout and components

215 *2.3. Optical path & imaging*

216 Figure 3 is a schematic representation of the engine test bed. The optical assembly is at the top right  
 217 corner. Fused quartz was chosen for the optical window as it has the appropriate mechanical, thermal and  
 218 optical properties. An adjustable first-surface Aluminum mirror passed the emitted light to the Nikon f2.8  
 219 Macro lens. The lens had the maximum diameter aperture setting to allow as much light into the camera  
 220 as possible. With the given focal length, the aperture setting, the subject distance and Circle of Confusion

221 the estimated depth of field (i.e. sharp region) is  $\pm 5$  mm. The Phantom V2.3 camera was set to record at  
 222 15 kHz. At this rate the exposure time was  $65 \mu\text{s}$  and the flame image was recorded in a  $256 \times 128$  pixel  
 223 array. Spatial and temporal resolution was found to be  $0.19$  mm/pixel and  $67 \mu\text{s}$  respectively. From the  
 224 camera's internal memory the images were sent to a PC in 24 bit bitmap format. The actual images had  
 225 only 256 greyscales but the analysing code worked faster with the larger, 24 bit bitmaps rather than the  
 226 memory saving 8 bit ones. These images were fed into a C language code for analysis, which after some  
 227 filtering and noise reduction determined the position of useful combustion cycles. The following geometric  
 228 properties were then calculated for each picture that contained useful data: area; perimeter; mass center  
 229 coordinates; x-y terminal points coordinates; best fit circle; best fit ellipse; circularity; roundness; solidity;  
 230 ratio of perimeters; and different shape factors.

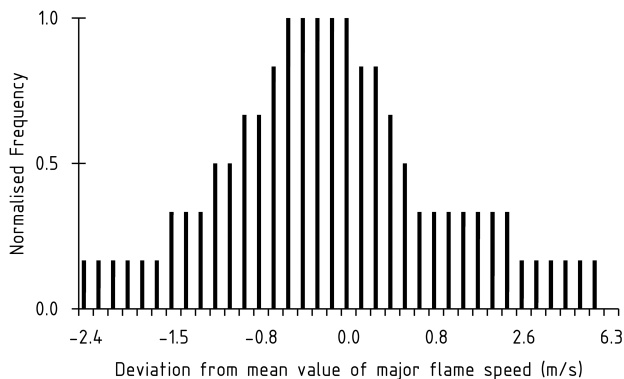


Figure 4: Sample data distribution, in this case for M85, 1200 rpm, CR=5.00, at  $804 \mu\text{s}$ ,  $S_{t=804} = (5.9 \pm 0.15)$  m/s

#### 231 2.4. Uncertainties

232 During recording, especially at the early stages of flame initiation, the experimental apparatus had to  
 233 capture flames with low light intensity for short times. Therefore, the optical set up was calibrated to its  
 234 highest sensitivity. This meant one of the major sources of uncertainties was light entering the optical path  
 235 from outside. The underground location of the laboratory helped to provide nearly complete darkness for the  
 236 tests. High-transparency window material and a high-reflectivity optical mirror were used, therefore errors  
 237 arising from scattering, absorption etc. were neglected. Errors from the CCD sensor and the computers  
 238 internal clock were also neglected. Changes in the air fuel mixture, quality of sparks, distance of engine and  
 239 CCD sensor were considered as random uncertainties. These arose from the combination of an infinitely  
 240 large number of infinitesimally small errors, which was expected to result in a normal frequency distribution,  
 241 according to the Central Limit Theorem in statistics [61]. Figure 4 is typical of statistical data obtained for  
 242 all conditions in this research. It illustrates that the data have a normal distribution, and that statistical  
 243 analysis of the data with normal-distribution statistics is a justified approach.



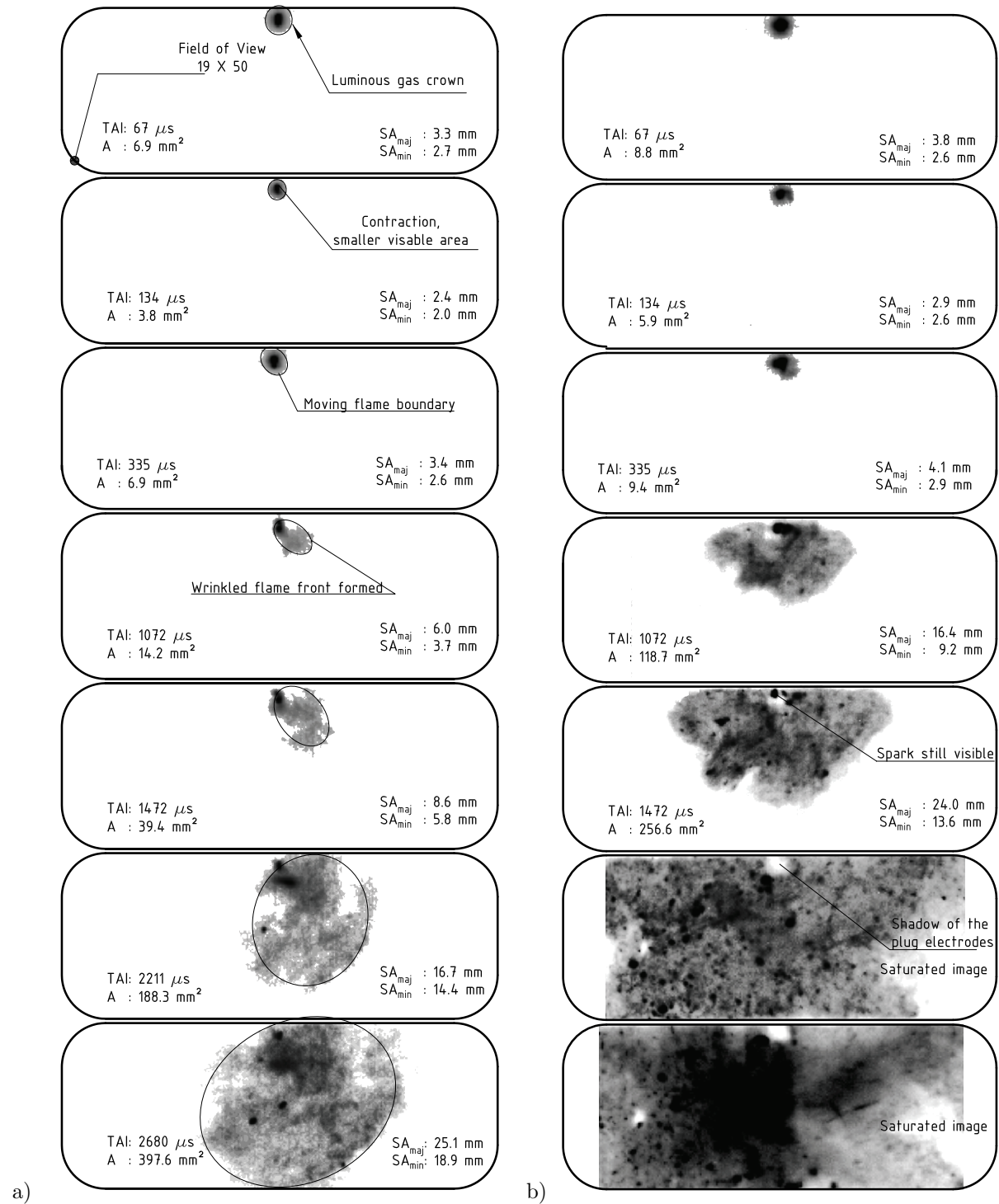


Figure 5: Sample flame images a, isooctane, conditions: 1200 rpm and CR=5.00 b, gasoline conditions: 1500 rpm and CR=5.00

### 244 3. Results & Discussion

245 The quantitative and direct comparison of flame speed measurements in optical engines is difficult. The  
 246 wide selection of fuels, operating conditions and the <sup>16</sup>optical engines themselves produce very different in-

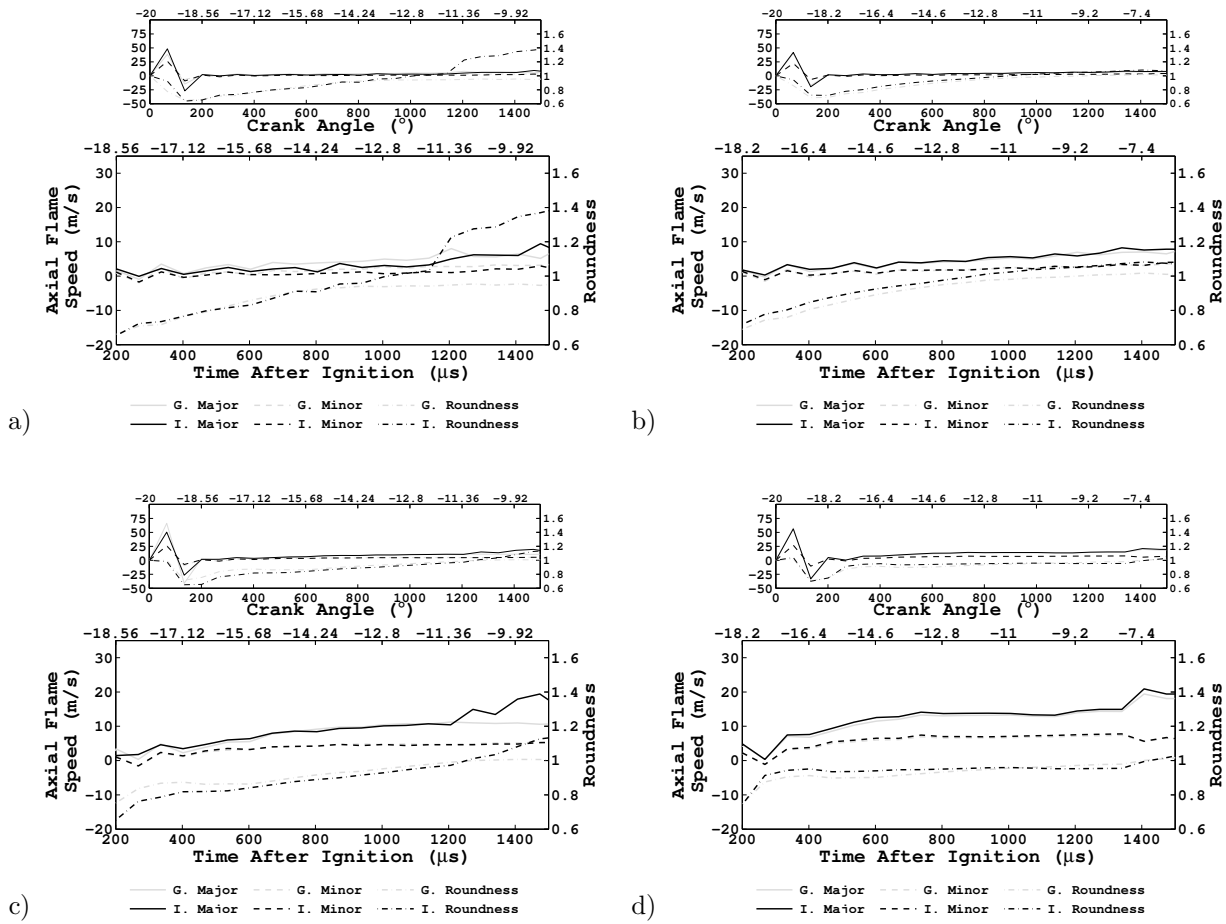


Figure 6: Flame speeds and roundness of Gasoline and Isooctane a, 1200 rpm and CR=5.00 b, 1500 rpm and CR=5.00 c, 1200 rpm and CR=8.14 d, 1500rpm and CR=8.14

Table 5: Derived flame speed values using the EQR method in different optical engines

Author	Reference	Engine Speed (rpm)	Fuel	Air/Fuel Ratio	CR	Combustion Chamber Geometry	$S_n$ (m/s) at 1000 $\mu s$ after ToI (Equivalent Radius Method)
Ihracska	-	1500	Isooctane	1.00	8.14	Rectangular	10.4
Ihracska	-	1500	Gasoline	1.00	8.14	Rectangular	10.3
Ihracska	-	1500	E85	1.00	8.14	Rectangular	9.1
Ihracska	-	1500	M85	1.00	8.14	Rectangular	14.4
Pischinger	[16]	1400	Propane	1.00	6.70	Square	4.1
Keck	[15]	1400	Propane	0.87	5.75	Square	6.1
Herweg	[31]	1250	Propane	1.00	7.30	Cylindrical	10.1
Aleiferis	[43]	1500	Isooctane	0.60	7.90	Pentroof	4.9
Aleiferis	[40]	1500	Gasoline	1.00	11.15	Pentroof	5.0
Aleiferis	[40]	1500	E85	1.00	11.15	Pentroof	4.0

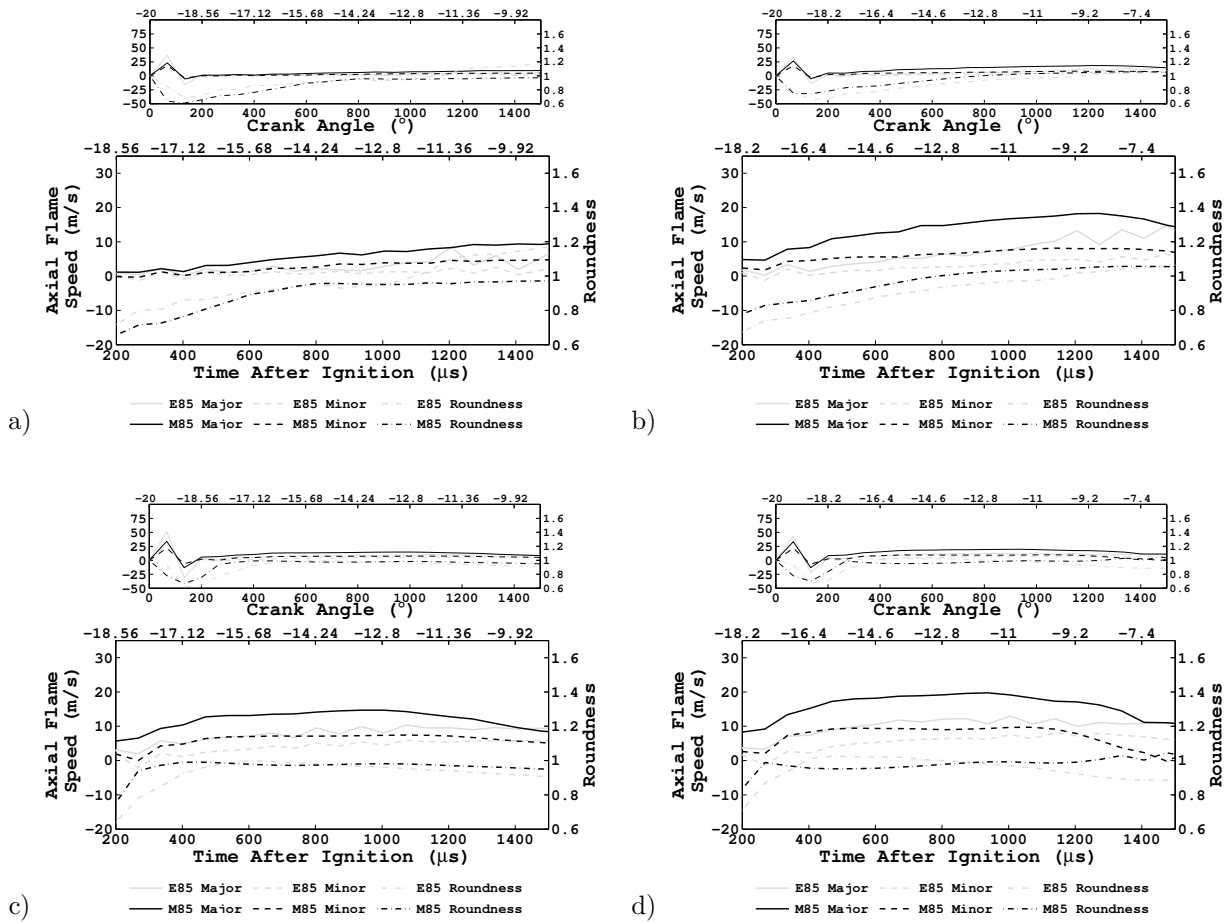


Figure 7: Flame speeds and roundness of E85 and M85 a, 1200 rpm and CR=5.00 b, 1500 rpm and CR=5.00 c, 1200 rpm and CR=8.14 d, 1500rpm and CR=8.14

247 cylinder conditions. Many parameters such as ignition modes [31], spark plugs [19], electrode gaps, valve  
 248 motion and timing [15] and engine geometries differ from engine to engine, not mentioning the operational  
 249 factors like engine speed or compression ratio, as shown in Table 1. Every factor, such as a relatively small  
 250 change of the direction of a spark plug electrode, could have significant effect on the flame development [18].  
 251 Therefore, the best comparison can be made between fuels or operating points if the data is collected from  
 252 the same engine with the same setup. For the purpose of comparison and cross discussion, the flame speed  
 253 was re-calculated from **therecorded** optical data based on the equivalence radius method, as summarized in  
 254 Table 5. Moreover, the comparison of flame shape is even more difficult as it is not only related to various  
 255 engine variables listed above but also to different modes of analysis. There are numerous methods have been  
 256 proposed in the literature to calculate shape parameters and there is still no consistency so far. For this  
 257 paper, Roundness was chosen as only the overall shapes was of interest and the local disturbances (wrinkling)  
 258 could not be captured accurately due to the limitation in the spatial resolution. No roundness data has  
 259 been found on in-cylinder flame in the literature. Table 5 shows the measured flame speed at a chosen time,

260 1000  $\mu\text{s}$  after ignition. Despite of different engine geometries and operating conditions, the flame speed has  
261 the same magnitude for each fuel. It should be noted that there are very few flame speed data available  
262 for early stages combustion in SI engines , especially those with satisfactory temporal resolution, a wider  
263 quantitative comparison appears impossible. Qualitatively, the flame speed trend obtained among different  
264 experiments is consistent. It has an initial high value due to the spark boosted combustion, followed by  
265 a minimum value that occurs between 200 and 500  $\mu\text{s}$ , and then a fairly steady increase until the end  
266 of the investigated period. Such a trend shows good agreement with the computational model of Herweg  
267 and Maly [42] for flame kernel formation in spark ignition engines. Considering the very different engine  
268 geometries, ignition modes and fuel mixing methods, the result is surprisingly well matched. **In addition,**  
269 **the flame speed measurement results of gasoline and E85 were compared to Aleiferis' findings [40]. It was**  
270 **found that the ratio of the flame speeds of these two fuels in the current study was similar to the one found**  
271 **in Aleiferis' work.** Gasoline showed a faster traveling flame by  $(19 \pm 6)\%$  at 1000  $\mu\text{s}$  after ignition. Apart  
272 from the absolute values, which shall be different among different work, the results are comparable, which  
273 suggests that the flame propagation characteristics are similar in SI engines for the earliest stages and is  
274 not engine geometry dependent. It is likely that the main controlling factor for early flame speed shall be  
275 the initial high energy input from the spark. Consequently, the finding of this study can be extrapolated to  
276 other engines.

277 **Isooctane and gasoline flames and some fitted ellipses are shown in Figure 5 at the condition of 1200,**  
278 **1500 rpm and CR = 5.00. The slowest flame propagation was observed at 1200rpm and CR = 5.00.** The  
279 last image is the 41<sup>st</sup> in the particular series where the traveling flame reaches the edge of field of view. In  
280 Figure 5 only seven images are shown. The first three are continuous with temporal resolution of 67  $\mu\text{s}$ .  
281 Then the next three were selected randomly, and the final one is the last image in the series. In 3D the  
282 flame boundary reached the combustion chamber long before it reached the edges of the visible area (Figure  
283 2). Considering the geometry of the combustion chamber, it was assumed that the flame speed vector in  
284 the z direction had always the same or smaller absolute values than the major flame speed vector at a given  
285 time. In the 3D space, the most distorted flames and the fastest ones did reach the combustion chamber  
286 walls and the piston at the end of the investigated period (1500  $\mu\text{s}$ ). However, for the vast majority of  
287 cases, there was no contact between the flames and the walls. When the contact did happen, a number of  
288 new variables should be added to the flame propagation equations to derive true values of flame speeds.  
289 However as there were only relatively small number of data points with contact and its area was small, the  
290 effect of it was considered as a small random error. **The visual analysis of the gathered images showed a**  
291 **distinct difference in the physical appearance of the two fuel types of hydrocarbons and alcohols blends.**  
292 **Less luminous flames were found for the latter and higher intensity was seen on images of isooctane and**  
293 **gasoline with local maximums randomly distributed. This is likely to be the result of the simpler and smaller**  
294 **molecule structure of the alcohols. As the longer chains of hydrogen and carbon atoms of isooctane and**

295 gasoline are required more time for breaking and complete burning, there was more unburnt carbon, soot,  
296 present in flames than in the case of alcohols. The higher soot concentration resulted in brighter flames.

297 Figure 6 shows roundness and flame speed along the major and minor axes plotted against time after  
298 ignition and CA degrees for gasoline and isooctane. Similarly Figure 7 for E85 and M85. In each plot the  
299 smaller graph shows the flame speed curve from time after ignition. Each curve reaches a maximum and a  
300 minimum value, which will be discussed later. The larger graphs show the same parameters after 200  $\mu\text{s}$   
301 after ignition, which is a more-stable region of flame development.

302 Figures 6 and 7 indicate that the visible flame area first expands and reaches maximum flame speeds of  
303 the order 50 m/s at about 67  $\mu\text{s}$ , then it contracts as indicated by minimum flame speeds of the order of  
304 -30 m/s at about 134  $\mu\text{s}$ , and then the flame speeds become positive again. This flame contraction soon after  
305 the beginning of ignition is caused by rapid endothermic dissociation of fuel molecules and the formation  
306 of radicals in the mixture [62–64]. In order to verify that this flame contraction did not occur because of  
307 effects of spark energy changes in time, or ionization of the gas by the spark plug, experiments were carried  
308 out of discharging the spark plug in air and analysing the perimeter of the visible luminous plasma with the  
309 same analysis as for the flame front with fuels (Figure 8). In this case the maximum and minimum “flame  
310 speeds” of the gas ionized by the spark plug are about 10 m/s. When the plasma stabilized 200  $\mu\text{s}$  after  
311 spark discharge its value of roundness remained stationary, around 0.75. This value describes the shape of  
312 the electric arc between the spark plug electrodes.

313 The values of the relative standard error (RSE) in major flame speed measurements were plotted in  
314 separate graphs for each fuel in Figure 9. Similar uncertainty values were found for minor flame speed and  
315 roundness (these figures are not included for brevity). In general uncertainty analysis showed that at lower  
316 speeds and CR the errors were higher, suggesting a worse air fuel mixing, bigger large scale eddies caused  
317 by lower level of turbulence and more spacious combustion chamber respectively, and higher coefficient of  
318 variation in these conditions. Variations in the energy of the spark caused higher uncertainty values near  
319 67  $\mu\text{s}$  after ignition. Mixture dissociation into radicals dominated flame propagation at times near 134  $\mu\text{s}$   
320 after ignition, resulting in lowering uncertainty values from those near 67  $\mu\text{s}$  after ignition. The exothermic  
321 processes dominate 200  $\mu\text{s}$  after ignition and later on. The relative magnitude of turbulent fluctuating  
322 velocity to flame speed affects uncertainty of measurements. Therefore when the flame speeds are lower  
323 (soon after 200  $\mu\text{s}$ ) the uncertainties are higher than when flame speeds are higher (e.g. near 1200  $\mu\text{s}$ ).  
324 Higher speeds and higher compression ratios promote better mixing, so that uncertainties are lower in these  
325 cases.

326 Figures 6 and 7 indicate that the flame front is not spherical. Figure 10 presents a comparison of the  
327 spherical and elliptical flame-propagation approaches. In Figure 10, the major and minor flame speeds and  
328 their average were plotted in the same graph with the flame speed calculated using the equivalent radius  
329 method. For most of the time investigated, the average speed was similar to the speed calculated from the

330 equivalent radius method but slightly larger, especially when there were larger differences in the major and  
331 minor speeds.

332 The flame shape and its changes in time are important information in the understanding and prediction  
333 of in-cylinder processes. Therefore the ellipse method can provide useful data for CFD and emissions  
334 predictions in studies of fuel-engine combinations, and engine design processes [65].

335 Flame speed and shape factor measurements showed that an ellipses described the contour of combustion  
336 better than circles in the first stages of combustion. About the first 800  $\mu$ s of propagation were severely  
337 affected by the spark causing well elongated flames. This phenomenon was not dependent on fuel or engine  
338 operating conditions. At time of ignition, the value of roundness was found to be close to unity in all cases,  
339 which was confirmed by images showing a circular glowing area. Then, when the initial high energy got  
340 absorbed, the projection of the flame was elongated as the arc and the roundness dropped to about 0.7.  
341 Finally, in all investigated cases the calculated value of shape factors started increasing and approaching  
342 unity again. There was no description available of the flow field but the phenomenon of the flame becoming  
343 more circular later was expected. There is always a larger flux of unburnt charge passes through planes that  
344 contain the major axis (or in a general case Ferets diameter) simply because of these cross sections have  
345 larger areas. This of course is not valid for uniform flows where there is just one plane for the charge to  
346 flow. In an internal combustion engine there are main directions of flows but as it is turbulent, it could be  
347 approximated as a highly random field. The changes in shape were found to be dependent on the engine  
348 conditions and fuel. Higher engine speeds and CRs appeared to cause rounder contours; fuels with faster  
349 flame speeds also tended to have more regular shapes. Utilizing the properties of the ellipse fitting method  
350 two flame speed values were calculated normal to each other. It was observed that changes in the magnitude  
351 of one flame speed component corresponded to the change in the magnitude of the other one. Therefore,  
352 these peaks were caused by a large scale in-cylinder process rather than some local disturbance.

353 Isooctane (major: 13.76, minor: 7.05) (all flame speed data have a unit of m/s and at condition of CR:  
354 8.14; 1500 rpm; 1000  $\mu$ s] and E85 (major: 12.97, minor: 7.55) were found to have more unstable behaviour in  
355 combustion; their flame speed curves had more fluctuations than the other two fuels. These two fuels showed  
356 the largest changes in shape, sometimes exceeding value of unity of their shape factors. It seemed that all  
357 fuels would sooner or later reach a fairly stable flame speed value depending on the operating conditions.  
358 The rate of stabilizing was found to be the lowest for isooctane, which in most cases had increasing flame  
359 speeds until the end of recording. In Table 6 all flame speed results are shown for each conditions and fuels.  
360 Moreover, in order to compare fuels directly to eachother the EQR method values were normalised to ones of  
361 isooctane. Similar flame speed values were measured for isooctane and gasoline (major: 13.20, minor: 6.70),  
362 and most of the time the trend of their change in flame shape showed agreement. As it can be seen from  
363 Figure 6 their flame speed curves were overlapping, apart from the earliest times which were associated with  
364 higher unceartainties. Their similarity was more obvious at higher speed and CR where the normalised

365 values showed only a couple of percentage difference but largest difference was only about 15%. In the case  
 366 of gasoline, the results were only informative as its chemical properties were not guaranteed. The highest  
 367 and most stable flame speeds were found in the case of M85 (major: 19.13, minor: 9.69) which reached  
 368 its stationary values first. Also, the roundest contours were recorded for this fuel, with fairly low errors in  
 369 the measurements. This might be a result of the higher flame speed as fluctuating and random in-cylinder  
 370 flows had less effect on the flame propagation. A large difference in flame speed was observed from the  
 371 other fuels especially for the low speed, CR measurements. It was an interesting to see the difference in the  
 372 behaviour of the two oxygenated fuel blends, while E85 seemed to be showing similar flame propagation  
 373 characteristics to isooctane, M85 clearly stood apart from E85. As the geometry of the combustion chamber  
 374 and the operating conditions were the same it is likely that this behaviour of M85 can be explained by the  
 375 combustion kinetics of methanol. The high laminar flame speed of methanol was explained on the basis of  
 376 the successive dehydrogenations of methoxyl radical by Veloo et.al. [66] per Ranzi et.al. [67]. Finally, Table  
 377 7 summarises the effect of different engine speeds and higher compression ratios on the flame speeds of the  
 378 tested fuels. In this table the values were normalised in order to provide an easy comparison between the  
 379 engine conditions. A general result is that flame speeds along the major axis are closer to the corresponding  
 380 maximum values than the ones along the minor axis. This is a direct result of the initially highly distorted  
 381 shapes becoming more circular as the minor axis elongated more during the flame development. It can be  
 382 seen that M85 produced somewhat different results from the rest of the fuels this is probably the result of  
 383 the aforementioned combustion kinetics. The normalised values for isooctane, gasoline and E85 were quite  
 384 similar (within about  $\pm 10\%$ ), indicating that the flame propagation characteristics of these fuels tend to  
 385 react similarly to changes of engine conditions.

Table 6: Flame speed values calculated using the EQR method and along the major and minor axes at 1000  $\mu$ s AIT, for an easy comparison of fuels the EQR method speed values were normalised to flames peeds values of isooctane

CR	Engine Speed	Isooctane				Gasoline				E85				M85			
		Major	Minor	EGR	Ratio to	Major	Minor	EGR	Ratio to	Major	Minor	EGR	Ratio to	Major	Minor	EGR	Ratio to
-	(rpm)	(m/s)	(m/s)	method	isooctane	(m/s)	(m/s)	method	isooctane	(m/s)	(m/s)	method	isooctane	(m/s)	(m/s)	method	isooctane
5.00	1200	3.10	1.21	1.57	1.00	2.48	1.36	1.80	1.15	2.87	1.30	1.91	1.21	7.29	3.88	4.95	3.15
5.00	1500	5.66	2.44	3.70	1.00	5.31	2.58	4.12	1.11	7.71	3.57	5.20	1.41	14.69	7.36	11.01	2.98
8.14	1200	10.11	4.70	6.90	1.00	10.45	4.70	7.05	1.02	8.03	4.42	7.14	1.04	16.74	7.63	11.84	1.72
8.14	1500	13.76	7.05	10.40	1.00	13.26	6.70	10.31	0.99	12.97	7.55	9.10	0.88	19.13	9.69	14.40	1.38

## 386 4. Conclusions

387 Flame propagation characteristics of isooctane, gasoline, M85 and E85 were recorded using a high-  
 388 specification camera in a specialty-designed optical-access engine. The high temporal-resolution pictures  
 389 were analysed with a purpose-built code and statistically compiled. In-cylinder combustion processes with

Table 7: Flame speed values along the major and minor axes at 1000  $\mu$ s AIT, for an easy comparison of the results from different engine conditions a normalised value is shown for each results and conditions

CR	Engine speed	Isooctane				Gasoline				E85				M85			
		Major ratio	Condition ratio	Minor ratio	Condition ratio	Major ratio	Condition ratio	Minor ratio	Condition ratio	Major ratio	Condition ratio	Minor ratio	Condition ratio	Major ratio	Condition ratio	Minor ratio	Condition ratio
-	(rpm)	(m/s)	-	(m/s)	-	(m/s)	-	(m/s)	-	(m/s)	-	(m/s)	-	(m/s)	-	(m/s)	-
5.00	1200	3.10	0.23	1.21	0.17	2.48	0.19	1.36	0.20	2.87	0.22	1.30	0.17	7.29	0.38	3.88	0.40
5.00	1500	5.66	0.41	2.44	0.35	5.31	0.40	2.58	0.39	7.71	0.59	3.57	0.47	14.69	0.77	7.36	0.76
8.14	1200	10.11	0.73	4.70	0.67	10.45	0.79	4.70	0.70	8.03	0.62	4.42	0.59	16.74	0.87	7.63	0.79
8.14	1500	13.76	1.00	7.05	1.00	13.26	1.00	6.70	1.00	12.97	1.00	7.55	1.00	19.13	1.00	9.69	1.00

390 these fuels were investigated in the visible spectra. The high-temporal resolution enabled evaluation of flame  
391 kernel formation. A new way of combustion analysis was proposed, where ellipses are used to model the  
392 projected flame boundaries. This method elucidated details of the combustion properties and added data to  
393 the existing literature on these four fuels. **To the authors' knowledge this is the first study on detailed flame  
394 speed measurements for M85 from optical engines.** Specifically it was concluded that:

- 395 1. The spherical flame propagation assumption has certain limitations. Results showed that for some  
396 cases the spherical flame front assumption is reasonably valid; but one needs to consider non-isotropic flame  
397 propagation in order to model in-cylinder processes more accurately. This is especially so for the earlier  
398 combustion stages when the spark causes highly distorted flame contours.
- 399 2. For all fuels the flames were more elliptic than circular immediately after ignition, which caused the  
400 least round flame-kernel shapes. In all cases, after the first 200  $\mu$ s, the elliptic shapes gradually became  
401 more circular.
- 402 3. Higher flame speeds were observed with increasing engine speed and compression ratio.
- 403 4. The standard deviation of the measured values, and uncertainty in values, decreased at higher speeds  
404 and compression ratios. Roundness and lower fluctuations of flame speed also indicated more stable flames  
405 at those conditions, as a result of higher flame speed, better mixing, and smaller large-scale eddies.
- 406 5. For all tested fuels at every operating condition a contraction of the flame was observed on the second  
407 recorded image. This is due to the endothermic process associated with the formation of radicals in the  
408 mixture.
- 409 6. The phenomenon of ignition delay can be defined for SI engines utilizing the observed flame-kernel  
410 contraction. Ignition-delay is defined as the time between spark ignition and establishment of the steadily  
411 expanding flame kernel.
- 412 7. A large number of sample observations were plotted. The distribution function showed good agreement  
413 with the normal distribution curve.
- 414 8. Isooctane and gasoline showed similar behavior from the flame propagation point of view, though  
415 gasoline produced more shape-invariant flames (uncertainties were lower and flames were more round). The  
416 results confirm isooctane (a pure chemical) is a suitable gasoline-blend surrogate as a baseline comparison



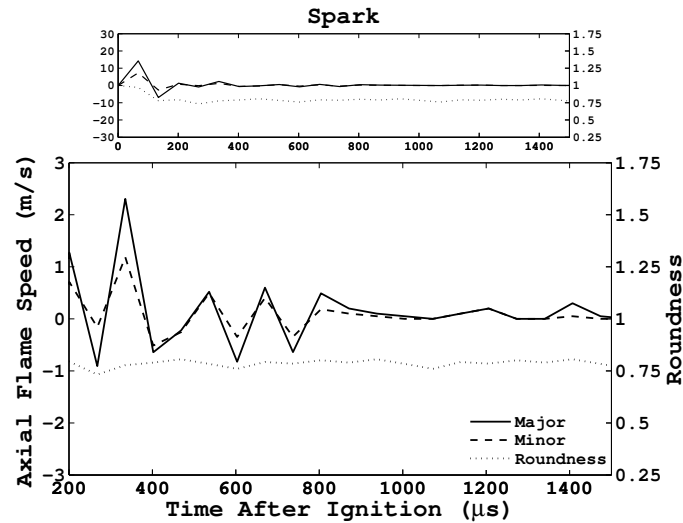


Figure 8: Flame speed measurement in air (no fuel admitted) at 1500 rpm and CR=8.14

417 fuel from a flame propagation point of view. M85 was found to have the fastest flame speed and the most  
 418 round boundaries. The flame speeds and roundness of the two alcohols were found to be different. In  
 419 contrast to M85s regularity and fast propagation, E85 showed more shape-variant burning and lower flame  
 420 speeds.

## 421 References

- 422 [1] N. Stern, *The Economics of Climate Change, The Stern Review*, Cambridge University Press, Cambridge, 2007.
- 423 [2] A. M. Namasivayam, T. Korakianitis, R. J. Crookes, K. D. H. Bob-Manuel, J. Olsen, *Applied Energy* 87(3) 769–778.
- 424 [3] T. Korakianitis, A. M. Namasivayam, R. J. Crookes, *International Journal of Hydrogen Energy* 35(24) 13329–13344.
- 425 [4] T. Korakianitis, A. M. Namasivayam, R. J. Crookes, *Progress in Energy and Combustion Science* 37(1) 89–112.
- 426 [5] T. Korakianitis, A. M. Namasivayam, R. J. Crookes, *Fuel* 90(7) 2384–2395.
- 427 [6] C. Rakopoulos, G. Kosmadakis, E. Pariotis, *International Journal of Hydrogen Energy* 35(22) 12545 – 12560.
- 428 [7] D. Veynante, L. Vervisch, *Progress in Energy and Combustion Science* 28(3) 193 – 266.
- 429 [8] J. Daintith (Ed.), *Dictionary of Physics*, Oxford University Press Inc., 5th edition, 2005.
- 430 [9] C. J. Rallis, A. M. Garforth, *Progress in Energy and Combustion Science* 6(4) 303–329.
- 431 [10] G. T. Kalghatgi, M. D. Swords, *Combustion and Flame* 49(1-3) 163–169.
- 432 [11] D. R. Lancaster, R. B. Krieger, S. C. Sorenson, W. L. Hull, *SAE International Journal* (760160).
- 433 [12] N. Ozdor, M. Dulger, E. Sher, *SAE Technical Paper* (940987).
- 434 [13] S. C. Bates, *SAE Technical Paper* (890154).
- 435 [14] S. C. Bates, *Combustion and Flame* 85(3-4) 331–352.
- 436 [15] J. C. Keck, J. B. Heywood, G. Noske, *SAE Technical Paper* (870164).
- 437 [16] S. Pischinger, J. B. Heywood, *SAE Technical Paper* (880518).
- 438 [17] R. Maly, *Spark Ignition: Its Physics and Effect on the Internal Combustion Engine*, Plenum Press, New York, pp. 91–129.
- 439 [18] P. G. Aleiferis, A. M. K. P. Taylor, J. H. Whitelaw, Y. Ishii, K. Urata, *SAE Technical Paper* (2000-01-1207).
- 440 [19] J. C. Keck, *Symposium (International) on Combustion* 19(1) 1451 – 1466.
- 441 [20] F. Matekunas, *SAE International Journal* (830337).

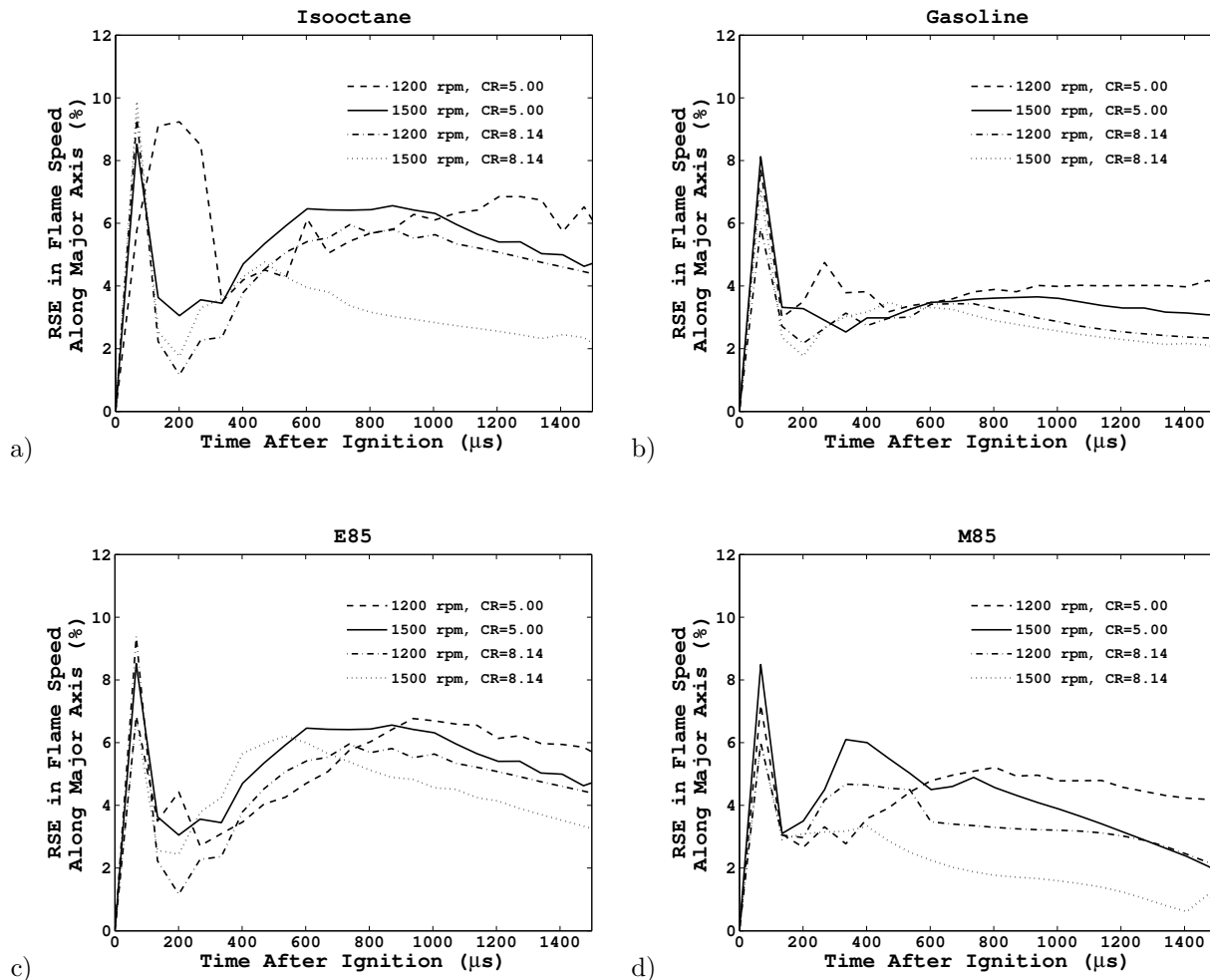


Figure 9: Errors in calculated flame speed along the major axis

442 [21] G. P. Beretta, M. Rashidi, J. C. Keck, *Combustion and Flame* 52(3) 217–245.  
 443 [22] L. Gillespie, M. Lawes, C. G. W. Sheppard, R. Woolley, SAE Technical Paper (2000-01-0192).  
 444 [23] D. Bradley, R. Hicks, M. Lawes, C. Sheppard, R. Woolley, *Combustion and Flame* 115(12) 126 – 144.  
 445 [24] J. F. Driscoll, *Progress in Energy and Combustion Science* 34(1) 91 – 134.  
 446 [25] A. O. zur Loye, F. V. Bracco, SAE Technical Paper (870454).  
 447 [26] J. B. Heywood, *Internal Combustion Engine Fundamentals*, McGraw-Hill, New York, 1988.  
 448 [27] M. Rashidi, *Combustion and Flame* 42(2) 111–122.  
 449 [28] J. B. Heywood, F. R. Vilchis, *Combustion Science and Technology* 38(5-6) 313–324.  
 450 [29] J. A. Gatowski, J. B. Heywood, C. Deleplace, *Combustion and Flame* 56(1) 71–81.  
 451 [30] A. Nakamura, K. Ishii, T. Sasaki, SAE Technical Paper (890322).  
 452 [31] G. Z. R. Herweg, *Proceedings of the Second International Symposium COMODIA* 90 173.  
 453 [32] H. Shen, D. Jiang, SAE Technical Paper (922239).  
 454 [33] P. G. Aleiferis, A. Taylor, K. Ishii, Y. Urata, *Combustion and Flame* 136(3) 283–302.  
 455 [34] K. Lee, J. Ryu, *Fuel* 84(9) 1116–1127.  
 456 [35] E. Conte, K. Boulouchos, *Combustion and Flame* 146(1-2) 329–347.

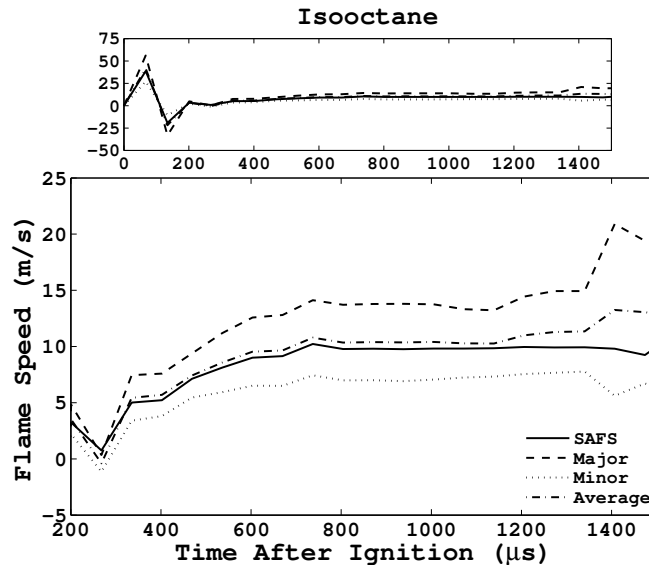


Figure 10: Comparison between the flame speed of isooctane with the spherical and elliptical methods. The results are similar for the other fuels.

- 457 [36] U. Gerke, K. Steurs, P. Rebecchi, K. Boulouchos, *International Journal of Hydrogen Energy* 35(6) 2566–2577.
- 458 [37] T. Tahtouh, F. Halter, C. Mounam-Rousselle, E. Samson, *SAE International Journal of Engines* (2010-01-1451).
- 459 [38] T. A. Baritaud, *SAE Technical Paper* (872152).
- 460 [39] J. Tagalian, J. B. Heywood, *Combustion and Flame* 64(2) 243 – 246.
- 461 [40] P. G. Aleiferis, J. Serras-Pereira, Z. van Romunde, J. Caine, M. Wirth, *Combustion and Flame* 157(4) 735–756.
- 462 [41] P. Aleiferis, J. Serras-Pereira, D. Richardson, *Fuel* (0) –.
- 463 [42] R. Herweg, R. Maly, *SAE Technical Paper* (922243).
- 464 [43] P. Aleiferis, Y. Hardalupas, A. Taylor, K. Ishii, Y. Urata, *Combustion and Flame* 136(1-2) 72–90.
- 465 [44] C. Crua, D. Kennaird, M. Heikal, *Combustion and Flame* 135(4) 475–488.
- 466 [45] C. Yang, H. Zhao, *International Journal of Engine Research* 11(6) 515–531.
- 467 [46] C. Yang, H. Zhao, *Combustion Science and Technology* 183(5) 467–486.
- 468 [47] H. Zhao, N. Ladommatos, *Engine Combustion Instrumentation and Diagnostics*, SAE International, 2001.
- 469 [48] S. C. Bates, *SAE Technical Paper* (892086).
- 470 [49] G. A. Olah, A. Goepfert, G. K. S. Prakash, *Beyond Oil and Gas: The Methanol Economy*, Wiley VCH, Weinheim, 2009.
- 471 [50] R. K. Niven, *Renewable and Sustainable Energy Reviews* 9(6) 535 – 555.
- 472 [51] A. K. Agarwal, *Progress in Energy and Combustion Science* 33(3) 233 – 271.
- 473 [52] A. e. a. J.S. Malcolm, P.G. Aleiferis, A study of alcohol blended fuels in a new optical spark-ignition engine, in *Internal*
- 474 *Combustion Engines: Performance, Fuel Economy and Emissions* by Institution of Mechanical Engineers, London, 2007.
- 475 [53] S. Turns, *An Introduction to Combustion: Concepts and Applications*, McGraw-Hill series in mechanical engineering,
- 476 McGraw-Hill Education, 2000.
- 477 [54] K. F. Mulchrone, K. R. Choudhury, *Journal of Structural Geology* 26(1) 143–153.
- 478 [55] R. Gonzalez, P. Wintz, *Digital Image Processing*, Addison-Wesley, Reading, MA, 1987.
- 479 [56] J. Russ, *The Image Processing Handbook*, CRC Press, Florida, 1999.
- 480 [57] Q. Ji, M. S. Costa, R. M. Haralick, L. G. Shapiro, *ISPRS Journal of Photogrammetry and Remote Sensing* 55(2) 75 – 93.
- 481 [58] A. Jain, *Fundamentals of Digital Image Processing*, Random House, New York, 1989.

- 482 [59] B. Jähne, *Digital Image Processing: Concepts, Algorithms, and Scientific Applications*, Springer-Verlag, Berlin, 1997.
- 483 [60] T. Anderson, *Multivariate Statistical Analysis*, John Wiley, 2nd edition, 1984.
- 484 [61] N. C. Barford, *Experimental Measurements: Precision, Error and Truth*, John Wiley and Son, 1994.
- 485 [62] T. Korakianitis, R. S. Dyer, N. Subramanian, *Journal of Engineering for Gas Turbines and Power*, Transactions of the  
486 ASME 126(2) 300–305.
- 487 [63] R. S. Dyer, T. Korakianitis, *Combustion Science and Technology* 179(7) 1327–1347.
- 488 [64] S. Sazhin, G. Feng, M. Heikal, I. Goldfarb, V. Goldshtein, G. Kuzmenko, *Combustion and Flame* 124(4) 684–701.
- 489 [65] T. Løvås, *Combustion and Flame* 156(7) 1348–1358.
- 490 [66] P. S. Veloo, Y. L. Wang, F. N. Egolfopoulos, C. K. Westbrook, *Combustion and Flame* 157(10) 1989 – 2004.
- 491 [67] E. Ranzi, A. Frassoldati, R. Grana, A. Cuoci, T. Faravelli, A. Kelley, C. Law, *Progress in Energy and Combustion Science*  
492 38(4) 468 – 501.

493 **List of Figures**

494 1 Illustration of the flame structure and temperature distribution of a flame, identifying the  
 495 reaction and preheat zones (The image was taken at 1200 rpm, CR 5.00, with iso-octane) . . . 4  
 496 2 Section and top views of combustion chamber with fitted ellipse to the flame front . . . . . 4  
 497 3 Schematic of the experimental rig: layout and components . . . . . 14  
 498 4 Sample data distribution, in this case for M85, 1200 rpm, CR=5.00, at 804  $\mu$ s,  $S_{t=804=}$   
 499  $(5.9 \pm 0.15)$  m/s . . . . . 15  
 500 5 **Sample flame images a, isoctane, conditions: 1200 rpm and CR=5.00 b, gasoline conditions:**  
 501 **1500 rpm and CR=5.00** . . . . . 16  
 502 6 Flame speeds and roundness of Gasoline and Isooctane a, 1200 rpm and CR=5.00 b, 1500  
 503 rpm and CR=5.00 c, 1200 rpm and CR=8.14 d, 1500rpm and CR=8.14 . . . . . 17  
 504 7 Flame speeds and roundness of E85 and M85 a, 1200 rpm and CR=5.00 b, 1500 rpm and  
 505 CR=5.00 c, 1200 rpm and CR=8.14 d, 1500rpm and CR=8.14 . . . . . 18  
 506 8 Flame speed measurement in air (no fuel admitted) at 1500 rpm and CR=8.14 . . . . . 24  
 507 9 Errors in calculated flame speed along the major axis . . . . . 25  
 508 10 Comparison between the flame speed of isoctane with the spherical and elliptical methods.  
 509 The results are similar for the other fuels. . . . . 26

510 **List of Tables**

511 1 Table of prior related publications . . . . . 7  
 512 2 Fuel properties . . . . . 8  
 513 3 Engine data . . . . . 9  
 514 4 Details of operating conditions . . . . . 11  
 515 5 Derived flame speed values using the EQR method in different optical engines . . . . . 17  
 516 6 **Flame speed values calculated using the EQR method and along the major and minor axes at**  
 517 **1000  $\mu$ s AIT, for an easy comparison of fuels the EQR method speed values were normalised**  
 518 **to flames peeds values of isoctane** . . . . . 22  
 519 7 **Flame speed values along the major and minor axes at 1000  $\mu$ s AIT, for an easy comparison**  
 520 **of the results from different engine conditions a normalised value is shown for each results**  
 521 **and conditions** . . . . . 23